THE ASTROPHYSICAL JOURNAL, 402:160–172, 1993 January 1

THE PARSEC-SCALE RADIO JET OF 4C 39.25

A. ALBERDI,[1] J. M. MARCAIDE,[1,2] A. P. MARSCHER,[3] Y. F. ZHANG,[3] P. ELÓSEGUI,[1,4]
J. L. GÓMEZ,[1] AND D. B. SHAFFER[5]

Received 1992 January 31; accepted 1992 July 9

ABSTRACT

Previous VLBI observations of the peculiar superluminal quasar 4C 39.25 at wavelengths $\lambda = 1.3$, 2.8, and 3.6 cm have revealed the presence of a superluminal component (*b*) moving between the western component (*c*) and the eastern component (*a*). Here we combine data published previously and reanalyzed by us with new VLBI observations between 1986 and 1989 at these wavelengths. Components *a* and *c* have remained fixed relative to each other, while component *b* has slowed down and brightened as it approaches component *a*. Our most recent $\lambda = 1.3$ cm VLBI observations have revealed the presence of a fourth, weak component (*d*) (to the west of *c*), which could be the core of the radio source, undetected in previous observations presumably due to an inverted spectrum and the limited dynamic ranges of the older maps.

These observational results support a model in which 4C 39.25 contains a bent relativistic jet which is misaligned relative to the observer near the core region, leading to a relatively low core brightness. Near the stationary components *c* and *a*, the jet curves its trajectory toward the observer, so as to become more closely aligned to the line of sight, while it is misaligned in the region between these two hotspots. We interpret component *b* as a shock wave propagating down the jet. This shock-in-curved-jet hypothesis is supported by the nonuniform proper motion of component *b*, the total and polarized flux density evolution of both the individual components and the source as a whole, the spectral evolution, and the relative position angles between the source components.

Subject headings: galaxies: jets — quasars: individual (4C 39.25) — shock waves — techniques: interferometric

1. INTRODUCTION

The 18th mag quasar 4C 39.25 (redshift $z = 0.699$; Hewitt & Burbidge 1980; Jackson 1990) is one of the strongest radio sources at centimeter wavelengths (8.9 Jy in 1990.5 at $\lambda = 2.8$ cm). At arcsecond scales the radio source structure consists of a very bright central core plus more extended structure elongated by about 4″ in the east-west direction, with a one-sided jet present along a position angle of 78° (measured from north to east) (Marcaide et al. 1989; Marscher et al. 1991). At milliarcsecond scales the structure is oriented toward the same general direction as the arcsecond-scale jet, as is the case in the majority of superluminal radio sources (Biretta & Cohen 1987).

A $\lambda = 6$ cm polarization map resulting from 1987.5 observations with the VLA shows that the easternmost component at arcsecond scales is polarized with a polarization position angle of 90°, while the compact, milliarcsecond-scale region is also polarized with a position angle of 100° (Marscher et al. 1991). However, an earlier $\lambda = 6$ cm VLA polarization map made by Kollgaard, Wardle, & Roberts (1990) shows that the polarization position angle of the central core at epoch 1983.8 was PA $\sim 175°$. The observed change in the polarization angle indicates that the magnetic field vector rotated from roughly parallel to the jet axis to a direction quasi-perpendicular to it over a period of less than 4 years. This rotation of the magnetic field vector in the most compact component is coincident with a major outburst in linearly polarized flux, which at $\lambda = 2$ cm increased 250% between 1983 and 1985 (Aller et al. 1985), and continued to increase at least through 1990 (Marscher et al. 1991).

In this paper we combine new high dynamic range VLBI maps of 4C 39.25 and its jet obtained at $\lambda = 1.3$, 2.8, and 3.6 cm between 1986 and 1989 with data published previously. We also present a model for the radio emission of extragalactic compact radio sources in terms of shock waves traveling along a relativistic jet, and we apply this model to interpret the observational results obtained for 4C 39.25.

2. OBSERVATIONS AND DATA REDUCTION

The VLBI observations at $\lambda = 1.3$ and 2.8 cm were made using the standard VLBI Mk II data recording system with a bandwidth of 1.8 MHz (Clark 1973). The VLBI observations at $\lambda = 3.6$ cm were done under the IRIS geodesy program with the Mk III (in mode B) system (see Rogers et al. 1983). 4C 39.25 was observed during these latter experiments over a sufficient number of scans to reconstruct its image or, at least, to fit the data by a model of spherical Gaussians.

We include in Tables 1 and 2 the general characteristics of the telescopes used in the VLBI observations reported here. The Mk II data were correlated at Max-Planck-Institut für Radioastronomie, Bonn, Germany, except data from epoch 1987.7, which were correlated at Caltech, Pasadena, CA. The data reduction was done in the standard form: (1) global fringe fitting, using the algorithm of Alef & Porcas (1986); (2) imaging using standard hybrid mapping procedures (Cornwell & Wilkinson 1981) employing the CLEAN algorithm (Högbom 1974). To obtain the characteristic parameters of the components in the maps, we also modeled the source using the minimum

[1] Instituto de Astrofísica de Andalucía, Apartado 3004, E-18080 Granada, Spain.
[2] Universitat de València, E-46100 Burjassot, Valencia, Spain (postal address).
[3] Department of Astronomy, Boston University, 725 Commonwealth Avenue, Boston, MA 02215
[4] Postal address: Harvard-Smithsonian Center for Astrophysics, 60 Garden Street, Cambridge, MA 02138.
[5] Interferometrics, Inc., 8150 Leesburg Pike, Vienna, VA 22182.

TABLE 1

CALIBRATION DATA FOR THE EXPERIMENTS: 4C 39.25

Antenna	Diameter (m)	Gain (K Jy^{-1})	T_{sys} (K)	λ (cm)	Epoch
Bonn	100	1.20	225	3.6	1983.4
		1.32	97	2.8	1987.7
		0.85	200	1.3	1988.7
		1.32	83	2.8	1988.7
		0.85	240	1.3	1989.7
Medicina	32	0.10	130	2.8	1986.2
		0.13	100	2.8	1987.7
		0.04	250	1.3	1988.7
		0.13	70	2.8	1988.7
Onsala	20	0.055	290	3.6	1983.4
		0.059	200	1.3	1988.7
		0.056	400	1.3	1989.7
Madrid	70	0.58	25	3.6	1983.4
Haystack	37	0.16	110	3.6	1983.4
		0.14	100	2.8	1986.2
		0.15	110	2.8	1987.7
		0.10	100	1.3	1988.7
		0.15	85	2.8	1988.7
		0.13	120	1.3	1989.7
Green Bank	43	0.20	114	3.6	1983.4
		0.28	85	2.8	1986.2
		0.28	80	2.8	1987.7
		0.06	110	1.3	1988.7
		0.28	150	2.8	1988.7
		0.06	160	1.3	1989.7
Owens Valley	40	0.21	75	2.8	1986.2
		0.21	70	2.8	1987.7
		0.12	70	1.3	1988.7
		0.21	159	2.8	1988.7
		0.12	90	1.3	1989.7
Fort Davis	26	0.04	110	3.6	1983.4
		0.09	240	2.8	1988.7
Hat Creek	27	0.07	180	2.8	1986.2
		0.07	79	2.8	1987.7
Pie Town	25	0.24	100	1.3	1989.7
Phased-VLA		1.20	125	1.3	1989.7
Kitt Peak	25	0.16	200	1.3	1989.7
Goldstone	70	0.58	274	3.6	1983.4

TABLE 2

CALIBRATION DATA FOR THE IRIS EXPERIMENTS: 4C 39.25

Antenna	Diameter (m)	Gain (K Jy^{-1})	T_{sys} (K)	λ (cm)	Epoch
Westford	18	0.0268	70.0	3.6	1986.2 (IRIS313)
		0.0268	80.0	3.6	1986.9 (IRIS366)
		0.0268	75.0	3.6	1987.7 (IRIS422)
Onsala	20	0.0489	190.0	3.6	1986.2 (IRIS313)
		0.0489	80.0	3.6	1986.9 (IRIS366)
		0.0489	90.0	3.6	1987.7 (IRIS422)
Fort Davis	26	0.0367	145.0	3.6	1986.2 (IRIS313)
		0.0367	150.0	3.6	1986.9 (IRIS366)
		0.0367	135.0	3.6	1987.7 (IRIS422)
Wettzell	20	0.0862	172.0	3.6	1986.2 (IRIS313)
		0.0862	50.0	3.6	1986.9 (IRIS366)
		0.0862	70.0	3.6	1987.7 (IRIS422)

number of elliptical Gaussians possible, comparing the results with the visibility data.

Some of the maps we present here have been published previously (Marcaide et al. 1989, 1990), but have been reanalyzed in the context of this paper. The new data correspond to the epochs 1988.7 and 1989.7 (at $\lambda = 1.3$ cm), 1988.7 (at $\lambda = 2.8$ cm), and 1986.2 and 1987.7 (at $\lambda = 3.6$ cm). The phased-array VLA plus the Pietown and Kitt Peak VLBA antennas took part in the 1989.7 observations at 1.3 cm, significantly enhancing the sensitivity.

The IRIS experiments suffer from such peculiarities as irregular (u, v) coverage, switched observations between different sources, etc., which make their calibration especially difficult. The source 1803+784 was chosen as the structure calibrator. Schalinski et al. (1990) have analyzed data at $\lambda = 3.6$ cm of 1803+784 from 10 different epochs between 1983.35 and 1987.7, showing that the structure during this period consisted of two components separated by a constant distance at each epoch.

3. OBSERVATIONAL RESULTS

3.1. *Observational History of 4C 39.25 at Milliarcsecond Scales*

The parsec-scale structure of the radio source 4C 39.25 was studied during the 1970s and 1980s by different authors using VLBI (Shaffer et al. 1977, 1987; Bååth et al. 1980; Pearson & Readhead 1984, 1988; Pauliny-Toth et al. 1981; Marcaide et al. 1985, 1989, 1990; Tang, Ronnang, & Bååth 1987; Marscher et al. 1987; Schalinski et al. 1988; Zhang et al. 1990; Alberdi et al. 1990; Alberdi 1991; Marscher et al. 1991). During the 1970s, the compact structure of 4C 39.25 at all three wavelengths consisted of two components separated by a distance of 2 mas with a position angle of 96° (measured from north to east and choosing the westernmost component—c—as reference).

Although the component separation was constant during the time period 1977–1982, their intensity ratio varied systematically. Indeed, while the total flux density was decreasing slowly but continuously, the flux density of the easternmost component was also decreasing, but the flux of the westernmost one was slowly increasing. In 1983 Marcaide et al. (1985) found a third component situated between the other two; they labeled the components a, b, and c from east to west, nomenclature that we will also use. The new component b was later found to be moving superluminally with a proper motion of 0.16 ± 0.02 mas yr^{-1}, as estimated by Shaffer et al. (1987), and of 0.18 ± 0.01 mas yr^{-1}, as estimated by Schalinski et al. (1988). From these proper motion measurements it can be estimated that component b was located in the vicinity of c at about 1980. During this time, the relative separation between components a and c has remained constant to within the accuracy of the measurements.

3.2. *VLBI Maps*

In Figure 1 we present sequences of maps of 4C 39.25 made at $\lambda = 1.3$ cm and at $\lambda = 2.8$ cm. We have arbitrarily aligned them at the position of component a. We also present a sequence of maps made at $\lambda = 3.6$ cm during the 1970s and 1980s, including for comparison a map from Bååth et al. (1980) at epoch 1973.8. These sequences suggest that the relative intensities of the components have been changing with time. From epoch 1982.6 on, the moving component (b) is present in the milliarcsecond structure at $\lambda = 2.8$ cm and 3.6 cm.

In the last two $\lambda = 1.3$ cm observing epochs a new component—which we designate as d—situated 2.6 mas west of component a is conspicuous. This new component was not required in the model for the source structure at epoch 1983.7; however, the sensitivity of that experiment to faint components was low, so it cannot be determined whether this component existed at a low level at that epoch. The existence of component d in the $\lambda = 1.3$ cm structure is clearly suggested from the very strong beating present in the visibility amplitudes and closure phases on the sensitive transcontinental baselines. Component d has a flux density $S_d \sim 120$ mJy and is placed 2.6 mas west of a, with a position angle with respect to b $\mathrm{PA}_{db} \sim -78°$. It is a very compact component with an angular size of ~ 0.15 mas.

We include in Table 3 the parameters of the best-fit models obtained by assuming that the source consists of multiple components with elliptical Gaussian brightness distributions and comparing the model visibilities to the data.

3.2.1. *Superluminal Motion of Component b and Relative Stationarity of Components a and c*

Using the maps obtained for 4C 39.25 at the different epochs, we have measured a proper motion of component b with respect to components a and c. In Figure 2 we show the time evolution of the angular distance between components a and c (θ_{ac}) and a and b (θ_{ab}). θ_{ac} remains constant to within the accuracy of the measurements, while θ_{ab} decreases quasi-uniformly with time. From a least-squares fit of a straight line to the data from all epochs we obtain a proper motion $\mu = 0.16 \pm 0.02$ mas yr^{-1} for b with respect to a. However, if we measure the proper motion only for the last five epochs, well calibrated and with quasi-simultaneous observations at two wavelengths, a proper motion of 0.11 ± 0.01 mas yr^{-1} is obtained. Thus, we observe a deceleration of component b as it approaches component a. This deceleration coincides with an increase of the total flux density as well as that of component b.

3.2.2. *Detection of Component d at $\lambda = 1.3$ Centimeters*

We have detected a fourth component (d) at $\lambda = 1.3$ cm. This new component could be identified with the central "core" of the superluminal source. If we adopt the relativistic beam model for compact radio sources, the core (observationally, the position where the expanding jet emission first becomes optically thin at a given frequency) must be very close to the central engine that is feeding the jet, i.e., west of component c. At $\lambda = 2.8$ and 3.6 cm d is not detected, owing to one or more of the following: (1) weak emission at these longer wavelengths because of self-absorption; (2) the low dynamic ranges of the maps; and (3) an unfavorable orientation of this portion of the jet with respect to the observer. In fact, if d were self-absorbed (e.g., with spectral index, $\alpha = 0.75$, where $S \propto \nu^{\alpha}$), it would have a flux density $S_{2.8} \sim 70$ mJy at $\lambda = 2.8$ cm, and even less at longer wavelengths.

Another argument in favor of d being the core of 4C 39.25 is that the distance between d and components a and c has remained constant between 1988.7 and 1989.7, while the distance between a and b has decreased from 0.56 mas to 0.44 mas. At the same time, the distance between b and d has increased from 2.06 mas in 1988.7 to 2.17 mas in 1989.7. This shift is essentially the same as that found for b with respect to a and c within our experimental precision. Therefore, we conclude that component b is moving, whereas d remains stationary with respect to a and c. Component d is therefore likely to

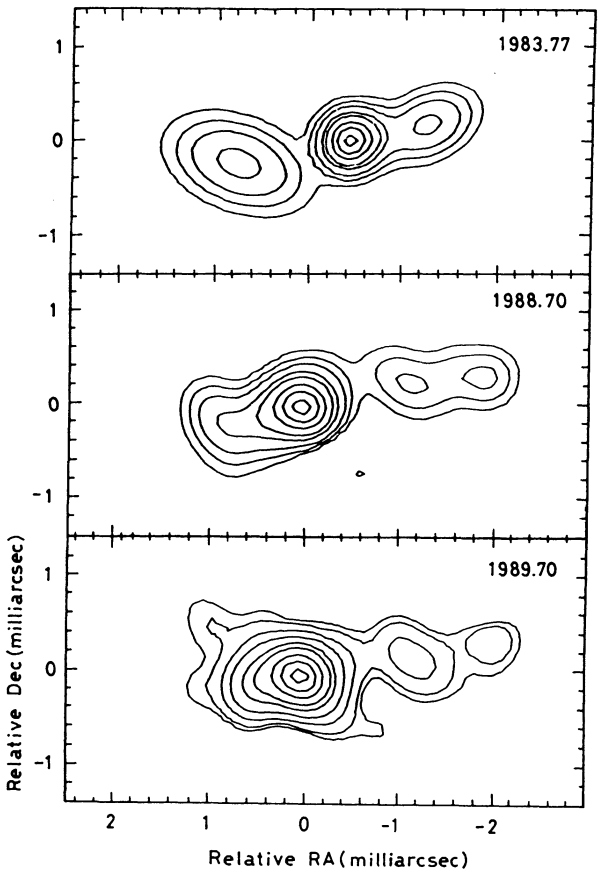

FIG. 1a

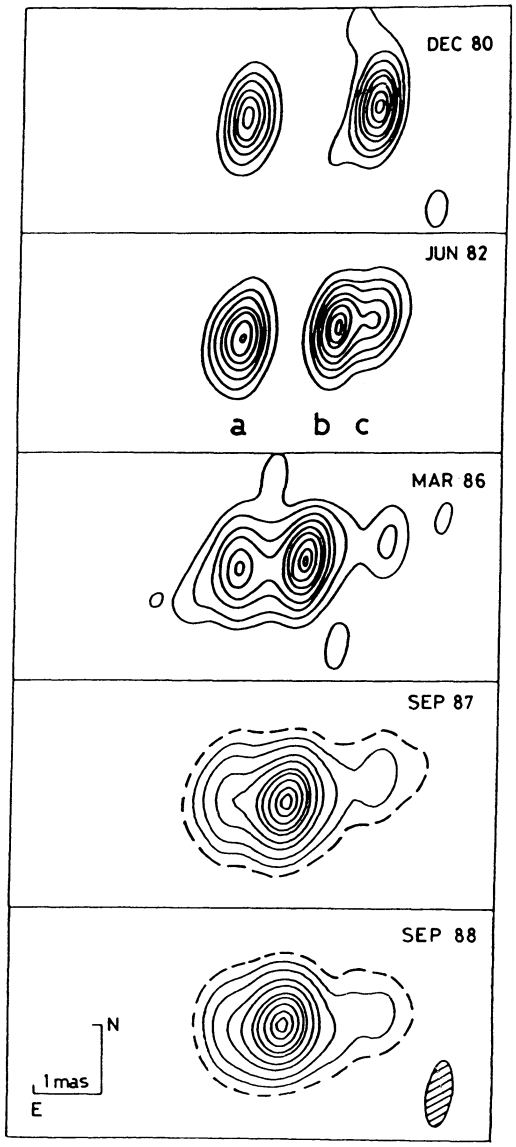

FIG. 1b

FIG. 1.—(*a*) Sequence of maps of the radio source 4C 39.25 at three wavelengths. All the maps have been arbitrarily aligned at the position of component *a*. (*a*) $\lambda = 1.3$ cm. The 1983.77 map is from model fitting (Marscher et al. 1987). The other two images are hybrid maps. The contours correspond to 2, 5, 10, 20, 30, 50, 70, 90% of the peak brightness. The maps have been convolved with a circular restoring beam of 0.4 mas. (*b*) $\lambda = 2.8$ cm. The contours correspond to 10, 20, 30, 45, 55, 70, 85, 95% of the peak brightness. In the last two maps two extra contours have been drawn at the 2% and 5% level. All the maps have been convolved with a restoring beam of 0.9 × 0.4 mas in PA −10°. (*c*) $\lambda = 3.6$ cm. The first map has been adapted from Bååth et al. (1980), with contour level spacing of 0.5 Jy (beam area)$^{-1}$ starting at 0.5 Jy (beam area)$^{-1}$. In the other maps, the contours correspond to 5, 10, 20, 30, 50, 70, 90% of the peak brightness. In the last epoch, one extra contour has been drawn at the 2% level.

be either the core or a third, noncore, stationary component similar to components *a* and *c*.

3.2.3. *Total and Component Flux Density Evolution*

In Figure 3 we present the total and individual component flux density evolution at centimeter wavelengths ($\lambda = 1.3$, 2.8, and 3.6 cm) during the 1980s. The total flux data correspond to measurements obtained primarily with the 100 m telescope at Effelsberg. The VLBI component flux densities are derived from model fits. Despite the large undersampling in time, it is clear that the radio light curve of component *b* follows the total flux density evolution, reaching a minimum around 1985 and increasing continuously from then on, whereas components *a* and *c* showed only slight flux density variability. Below, we identify this increase in flux density with the progressive alignment of component *b* with respect to the observer.

3.2.4. *Time Evolution of the Spectrum and Polarization of 4C 39.25*

There is limited information concerning the polarized flux density evolution. Aller et al. (1985) published data covering the time period from 1967 to 1985. They found that the polarized flux increased by 250% at $\lambda = 2$ cm from 1983 to 1985. This implies that the magnetic field became more ordered during this time. From 1985 to 1990 the polarized flux continued to increase (Marscher et al. 1991). This behavior is consis-

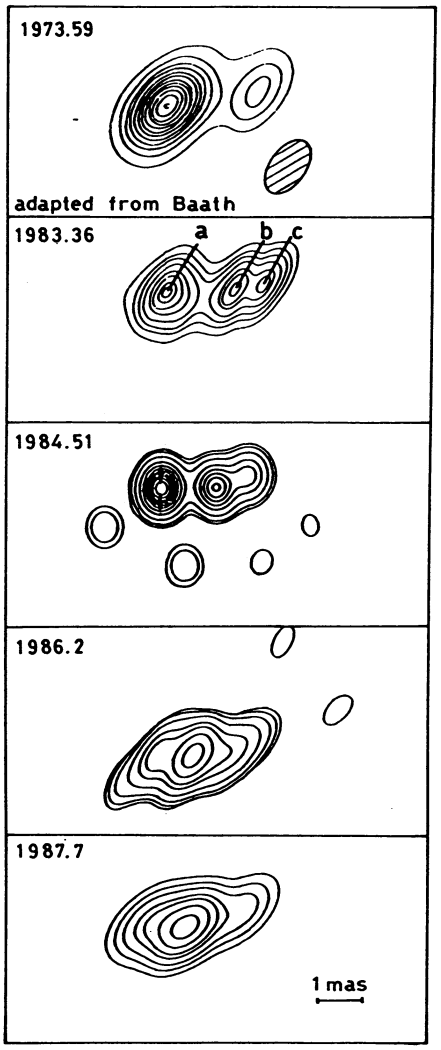

FIG. 1c

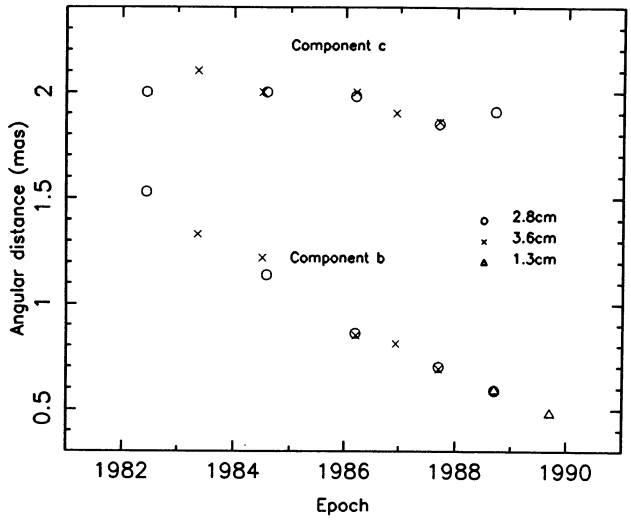

FIG. 2.—Angular separation between components *a* and *c* (θ_{ac}), and between components *a* and *b* (θ_{ab}), in milliarcseconds, as a function of observing epoch.

tent with the identification of component *b* as a relativistic shock wave traveling along the jet. A shock wave would strengthen the perpendicular component of the magnetic field, producing a net increase in polarized flux density.

From the flux density measurements made from 1983 to 1990, it is possible to study the temporal evolution of the turnover frequency, ν_m, and the flux density at this frequency, S_m. In fact, S_m almost doubled its value while ν_m remained essentially constant (Marscher et al. 1991). This behavior is consistent with the curved relativistic jet hypothesis discussed below.

4. INTERPRETATION

4.1. *Theoretical Model for 4C 39.25*

The majority of compact extragalactic radio sources observed at milliarcsecond resolution consist of a compact core with a knotty jet extending to one side (see, e.g., Zensus & Pearson 1990). The standard working hypothesis explains this morphology in terms of a relativistic plasma flowing in a narrow-angle cone (a "relativistic jet"), with shock waves producing the moving knots (Blandford & Königl 1979; Marscher 1990). According to this model, the predominant emission in the knots comes from the shocked gas: the component of the magnetic field parallel to the shock front is amplified, and the density and energy of the relativistic particles are increased, producing enhanced emission. Since 4C 39.25 has a superluminal knot (component *b*), we adopt the relativistic jet model as the basic explanation of its structure. However, the absence of a compact, flat-spectrum core (Marscher et al. 1987) and the presence of stationary features require modifications to the basic model. There are several arguments which suggest that *b* follows a curved trajectory as a function of time. Hence, we will consider a model in which the jet curves its trajectory by several degrees.

Marcaide et al. (1989) proposed a bent-jet model for the

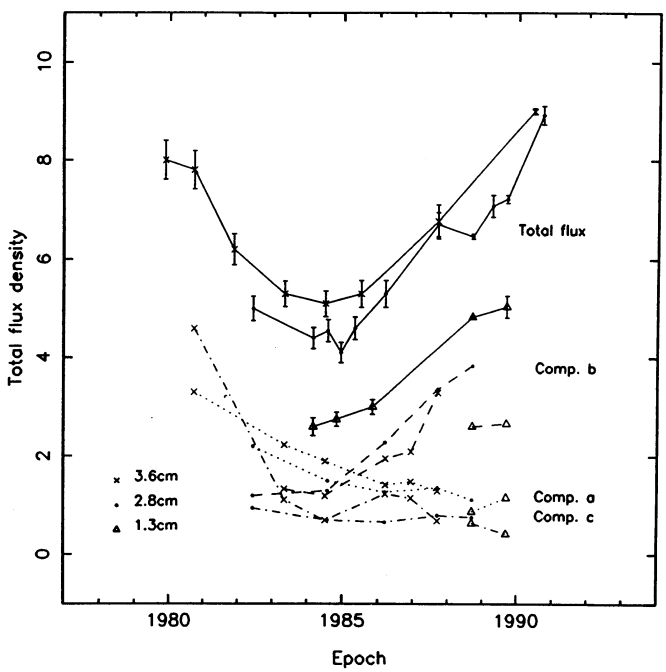

FIG. 3.—Total (*solid line*) and component flux density (in Jy) vs. time: component *a* (*dotted line*), component *b* (*dashed line*), and component *c* (*dot-dashed line*).

TABLE 3

RESULTS OF MODEL FITTING TO THE STRUCTURE OF 4C 39.25

Epoch	λ (cm)	Component	S (Jy)	θ_{ib} (mas)[a]	PA_{ib}[b]	Angular size	ϕ
1986.19.....	2.8	*a*	1.27	0.86	90	0.47 × 0.46	90°
		b	2.28	0	0	0.43 × 0.39	90
		c	0.66	1.20	−73	0.50 × 0.49	90
1986.19.....	3.6	*a*	1.42	0.85	85	0.68 × 0.54	34
		b	1.95	0	0	0.44 × 0.10	70
		c	1.24	1.08	−77	0.90 × 0.70	95
1986.94.....	3.6	*a*	1.48	0.81	85	0.86 × 0.36	45
		b	2.10	0	0	0.49 × 0.28	80
		c	1.15	1.06	−87	0.92 × 0.83	72
1987.70.....	2.8	*a*	1.36	0.70	86	0.60 × 0.50	30
		b	3.36	0	0	0.43 × 0.20	80
		c	0.80	1.15	−76	1.30 × 0.35	109
1987.70.....	3.6	*a*	1.29	0.69	83	0.76 × 0.24	106
		b	3.29	0	0	0.54 × 0.14	107
		c	0.69	1.17	−74	0.90 × 0.20	113
1988.70.....	1.3	*a*	0.88	0.59	92	0.32 × 0.12	100
		b	2.61	0	0	0.32 × 0.28	95
		c	0.64	1.34	−80	0.48 × 0.30	90
		d	0.22	2.06	−80	0.17 × 0.05	130
1988.70.....	2.8	*a*	1.12	0.59	86	0.59 × 0.40	32
		b	3.83	0	0	0.44 × 0.15	75
		c	0.76	0.94	−86	1.06 × 0.40	92
1989.70.....	1.3	*a*	1.16	0.48	94	0.36 × 0.18	−10
		b	2.66	0	0	0.28 × 0.15	62
		c	0.42	1.17	−80	0.60 × 0.48	116
		d	0.11	2.17	−78	0.05 × 0.02	167

[a] Angular distance of the *i* component with respect to *b*.
[b] Position angle of the *i* component with respect to *b*.

compact radio structure of 4C 39.25. In this model, the source represents a relativistic jet that bends owing to nonaxisymmetric external pressures, resulting in the formation of standing shocks, which are associated with the stationary components *a* and *c*. As a result of our numerical simulations, we found out that the standing shocks are not strictly necessary to produce enhanced emission at the positions of the components *a* and *c* if the jet is slightly reoriented with respect to the observer. Hence, we revised the model and considered components *a* and *c* as associated to regions of curvature of the jet at which the jet bends toward the line of sight. The relativistic Doppler boosting factor δ depends on the Lorentz factor γ and the angle θ between the velocity vector and the line of sight: $\delta = [\gamma(1 - \beta \cos \theta]^{-1}$. The dependence on orientation angle θ leads to a differential Doppler boosting between different positions of a curved jet (Marscher, Gear, & Travis 1990). This model is fully compatible with the model of Marscher et al. (1991) in which components *a* and *c* are sites where a jet, which perhaps follows a helical pattern, twists toward the line of sight. In both versions of this model, the moving component *b* corresponds to a shock traveling down the jet. As pointed out by Marcaide et al. (1990) and Marscher et al. (1991), the interpretation of *b* as a shock wave propagating along the jet explains the light curves of the total, as well as the polarized, radio flux density since 1980. For the remainder of this paper we adopt the corrected version of the bent-jet model as our working hypothesis.

From the observational results that we have presented, we can place some constraints on our model for the parsec-scale radio jet of 4C 39.25 based on the observed proper motion of component *b*. If we consider the observational data available from 1980 to 1990 for the angular distance between components *a* and *b*, we obtain a proper motion $\mu = 0.16 \pm 0.02$ mas yr^{-1}, which yields a value for the apparent velocity (in units of the speed of light *c*) $\beta_{app} = 3.60$, a maximum angle with respect to the observer $\theta_{max} = 31°$, and a minimum value for the Lorentz factor $\gamma_{min} = 3.74$, which corresponds to $\beta_{min} = 0.9635$ (we adopt the following values for the cosmological constants: $H_0 = 100$ km s^{-1} Mpc^{-1} and $q_0 = 0.5$). If we consider now the observed values for the angular separation between components *a* and *b* since 1986.21, we obtain a proper motion $\mu = 0.11 \pm 0.01$ mas yr^{-1}, which yields a value for the apparent velocity $\beta_{app} \lesssim 3$, a maximum angle with respect to the observer $\theta_{max} \sim 44°$, and a minimum value for the Lorentz factor $\gamma_{min} = 2.3$, which corresponds to $\beta_{min} = 0.897$.

In this model the source core should be closer to the location of the central engine that feeds the jet than are components *a*, *b*, and *c*, and therefore should lie to the west of component *c*. The core is absent on the maps at $\lambda = 2.8$ cm and 3.6 cm, probably due to the inverted spectrum of the core and to the insufficient dynamic range of the maps. We think that the new component found at $\lambda = 1.3$ cm, *d*, could be the core of the radio source. From the two maps at $\lambda = 1.3$ cm (see Fig. 1*a*) we have not detected a proper motion of component *d* with respect to *a* and *c*, which is in favor of *d* being the core of the radio source and argues against the possibility of *d* being a new *b*-type moving component. However, a moving knot can have a low proper motion if its trajectory is closely aligned to the line of sight, as occurs near components *a* and *c* according to our model. In fact, Goran Sandell (private communication) has reported that 4C 39.25 has flared at 1.1 mm, increasing its flux density from 0.9 ± 0.1 Jy (1990 September) to 1.8 ± 0.12 Jy

(1991 May). This outburst could represent the birth of a new component that would eventually appear in the VLBI structure. On the other hand, measurements at the JCMT in 1991 August at wavelengths of 0.8, 1.1, 1.3, and 2.0 mm (S. Bloom, A. P. Marscher, & W. K. Gear, private communication) are consistent with a $\sim \nu^{-0.6}$ spectrum from 10 to 350 GHz. These latter data argue against a new, high-frequency component.

4.2. *Numerical Simulations of the Total and Polarized Flux Density of a Bent Relativistic Jet with a Moving Shock Wave*

In order to model the superluminal component (*b*) in 4C 39.25 we consider a plane hydrodynamic shock wave travelling along a bent supersonic jet with a power law distribution of relativistic electrons. The following assumptions and approximations are made:

1. The direction of the magnetic field at each point of the quiescent region of the jet is mainly random, and the flow in this region is parallel to the jet axis. The magnetic field strength is assumed to fall off with radius according to the power law $B \propto r^{-q}$.
2. The "heated" gas flows uniformly, with constant speed, parallel to the jet axis. The emitting volume—that occupied by the shocked gas—expands laterally as it moves down the jet.
3. We assume an ultrarelativistic equation of state (adiabatic index $\Gamma = 4/3$) both up- and downstream of the shock wave. This implies that the bulk flow speed of the jet should increase downstream in the jet as internal energy is converted into bulk motion, contrary to observation. If the jet is composed of relativistic electrons and nonrelativistic protons, the flow speed will be constant, but the corresponding value $\Gamma = 13/9$ does not admit analytical solutions to the shock jump conditions. We therefore use $\Gamma = 4/3$ as an approximation to the more self-consistent case of $\Gamma = 13/9$.
4. Under the influence of the shock, the synchrotron emitting gas is compressed and its emissivity is enhanced. Our model assumes that the electrons are heated only by compression, and that the jet is evolving adiabatically.
5. In principle, when there is a prolonged disturbance in a jet, a reverse and a forward shock are produced. The reverse shock is produced when the flow velocity for the shocked region in less than the velocity of the enhanced jet flow (the "driver gas"), but both of these are greater than the velocity of the old, quiescent flow. In our previous description we have restricted ourselves to reverse shocks, and we will do so hereafter, since, as we discuss later, the compact VLBI structure of 4C 39.25 is difficult to explain through the use of forward shocks.

Under these conditions, we can integrate the transfer equations that characterize the propagation of synchrotron radiation through a cosmic plasma. If we approximate that the real source is composed of a superposition of elementary homogeneous sources (cells), we can solve the transfer equations for each of the cells. The value obtained for the intensity in a cell is taken as the incident value for the next cell to be integrated. The propagation of the synchrotron radiation in a region can be fully described by the parameters: magnetic field B, which falls off as $B \propto r^{-q}$ and makes an angle θ_B relative to the line of sight; relativistic electron density per unit energy $N(E) = N_0 E^{-s}$, with $N_0 \propto r^{-2(s+2)/3}$; and observing frequency $\nu_{\rm obs}$.

We can describe the physical parameters of the shocked region relative to those of the preshocked gas through the jump conditions across the shock front. The first condition is that the number of particles for an element of fluid crossing the shocked and quiescent regions must be constant. In that sense, if we characterize the upstream, unshocked flow ahead of the shock front by a density n'_u, a velocity β'_u, and a Lorentz factor γ'_u (with respect to the shock wave reference frame), and the downstream flow by the physical parameters n'_d, γ'_d, and β'_d, we can define a compression factor k as the ratio between the upstream and downstream densities. Considering the ultrarelativistic equation of state and working in the shock-front frame, we can define this compression ratio as a function dependent only on the Lorentz factor in the upstream flow (Blandford & McKee 1976; Königl 1980; Hughes, Aller, & Aller 1989, 1990). Thus, a unit length is compressed to a length k. The compression and deceleration of the shocked gas have primarily two consequences:

1. The component of the magnetic field perpendicular to the jet axis is enhanced by a factor $1/k$.
2. There is a change in the particle density between the upstream and downstream flows, as well as an energization of the particles passing through the shock front. Assuming that the gain of energy in the shock is due to adiabatic compression, the gain for each particle is proportional to $k^{-1/3}$. This, combined with the increase in particle density by a factor k^{-1} gives a factor $k^{-(s+2)/3}$ increase in N_0 across the shock front.

The jet plus shock wave flow is therefore completely described once we know the following parameters: the flow speed for the quiescent area (which determines the compression factor) $\beta'_{u,\rm sh}$, in the reference frame of the shock front; the velocity of the shock front in the observer's frame $\beta_{\rm sh}$; the size of the shocked area $L_{\rm sh}$; and the power-law index of the electron distribution s. The extent of the shock $L_{\rm sh}$ is difficult to estimate owing to the absence of time-dependent relativistic gas dynamic calculations. We therefore leave it as a free parameter.

In our code, we consider a conical jet formed by slabs, each with a width that increases linearly with distance r along the jet. We approximate that the emitted radiation propagates in a direction perpendicular to the jet axis in the rest frame of each slab of the jet (and directed toward the line of sight owing to relativistic aberration). We take five integration lines in each slab and 100 points on each of these lines and solve the transfer equations at each point. This method is essentially valid when the jet opening angle is narrow (opening half-angle $\phi \lesssim 4°$), which avoids large errors for any combination of the Lorentz factor γ and jet orientation angle θ, and diminishes the effects of differential Doppler boosting across a slab. Therefore, when solving the transfer equations, we assume as input value for the intensity at each point the value of the intensity in the previous one. The total flux density for a slab is the integration of the flux density of all the lines of a slab, an integration that we make using Simpson's rule.

If the Doppler factor of the shock frame with respect to the observer is $\delta_{\rm sh}$ and the Doppler factors of the upstream and downstream flows in the shock frame are $\delta'_{u,\rm sh}$ and $\delta'_{d,\rm sh}$, the Doppler factors of the upstream and downstream flows in the observer's frame are $\delta_{\rm sh}\delta'_{u,\rm sh}$ and $\delta_{\rm sh}\delta'_{d,\rm sh}$, respectively. These factors give the transformation law to obtain the frequency in the plasma frame for a given frequency of observation.

The component of the magnetic field parallel to the jet axis varies as $B_{\parallel} \propto r^{-2}$, while the perpendicular component varies as $B_{\perp} \propto r^{-1}$. Remembering that only the perpendicular

component is enhanced by a transverse shock wave, we can assume that the r^{-1} term dominates in the shocked region. For each point, the magnetic field has essentially two contributions: a randomly oriented component, and a component parallel to the flow direction, which is a fraction of the random field. However, we have introduced in our code a general dependence of the form $B \propto r^{-q}$.

The results we have described refer to the evolution of the total and polarized flux densities as a function of distance along the jet at each time. We also integrate the flux density along the whole jet at each time, and characterize the time evolution of the source flux as a whole.

The following are the main results obtained with our code:

1. The presence of a shock wave in the supersonic jet implies the appearance of rapid events in the total flux density light curve. These events are stronger with respect to the quiescent emission in polarized flux density than in total flux density.

2. When there is a shock wave travelling along the jet, the total flux density light curves have a strong frequency dependence, showing a shift in the position of the maximum from higher to lower frequencies.

3. The flux outbursts are more prominent with respect to the quiescent flux at higher frequencies.

4.3. *Application to the Radio Source 4C 39.25*

We have applied the code described above to the radio source 4C 39.25. There is evidence of the existence of a curved jet in 4C 39.25 which complicates the selection of the jet parameters due to the superposition of shock waves and geometric effects on the total flux and linear polarization. Also, since component *b* is increasing in flux density as it moves downstream, expanding adiabatically, the geometric effects must be important enough to compensate for the decreasing emissivity that accompanies expansion.

The model must be able to explain the following experimental results: the time evolution of the total and component flux densities, the stability of the relative distance between components *a* and *c*, the deceleration of component *b*, the time evolution of the apparent velocity β_{app}, the detection of component *d* at 1.3 cm, and the nondetection of this component at 2.8 cm.

We have also looked for a geometry appropriate to reproduce the experimental light curves of 4C 39.25 through a model in which the jet axis orientation results from precession, choosing different values of the precession angle and rate. However, we have not found any combination of these two parameters that reproduces the experimental results. We have derived instead a stationary geometry compatible with the experimental data. In Figure 4 we show the jet orientation relative to the observer versus distance along the jet as required by our model. We also show the projected jet trajectory. This trajectory shows a jet pointing quite close to the observer at certain points, as expected for one of the strongest radio sources at centimeter wavelengths, since smaller angles maximize the Doppler boosting. Notice also that the jet bends by $\sim 6°$, which could be explained by macroinstabilities (Hardee 1990), which do not disrupt the jet. This geometry, together with a shock wave velocity $\beta_{sh} = 0.967$, produces the apparent velocity versus jet distance relationship down in Figure 5, which reproduces the observed behavior of the superluminal component.

Knowing β_{sh} and the velocity of the nonshocked flow in the observer's frame, it is possible to determine the boosting

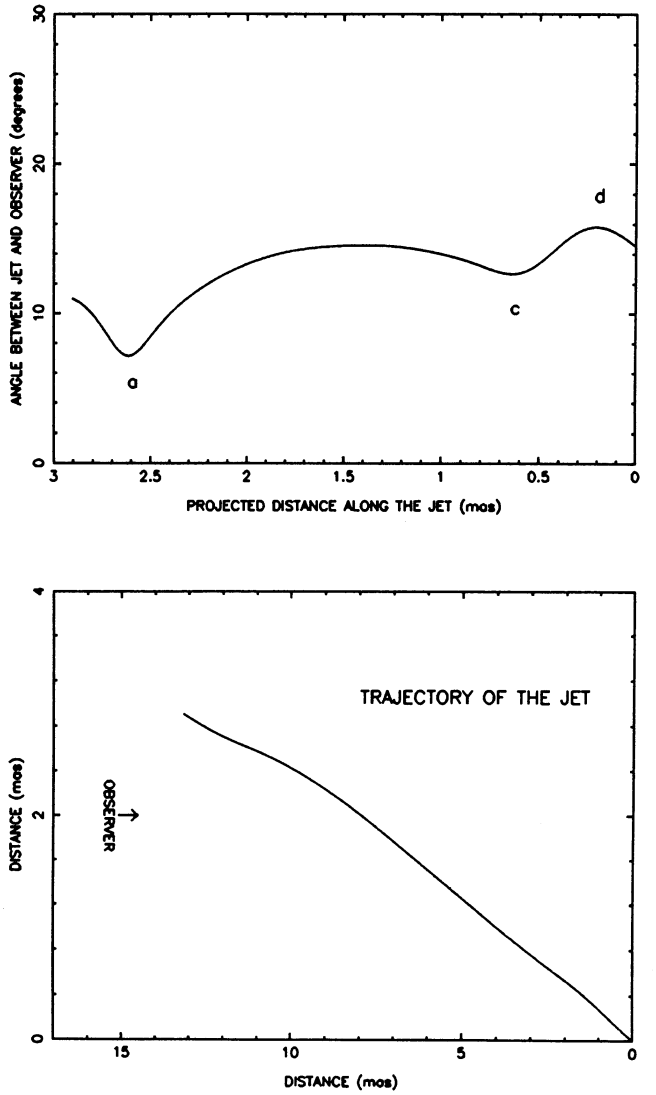

FIG. 4.—Angle between the jet and the observer in the source model for 4C 39.25, and trajectory of the jet with respect to the observer.

factors both for the shocked and the unshocked areas. We can reproduce the experimental results with a value $\beta_{u,obs} = 0.9965$. From the boundary conditions in the shock front, we can calculate the velocity of the shocked gas, yielding a value $\beta_{d,obs} = 0.9861$. We show in Figure 6 the ratio between the velocities of the two regions, adopting in both cases the geometry shown in Figure 4. The boosting is stronger for the shocked area than for the quiescent area, except for the region close to *a* where they have comparable values. At this position the angle to the observer is so small that the Doppler factor $\delta \sim 1/(1 - \beta)^{1/2}$ is nearly independent of θ and is stronger for the upstream flow than for the downstream flow since $\beta_{u,obs} > \beta_{d,obs}$.

In the models discussed above, we have considered only reverse shocks. We have also tried to reproduce the structure of the compact radio source considering forward shocks, but have not found any parameter set able to simulate the source structure. If we maintain the same values for the compression factor and for the shock front speed as in the case of the reverse shocks, the new upstream and downstream velocities in the observer frame would be $\beta_{u,obs} = 0.73$ and $\beta_{d,obs} = 0.901$, which

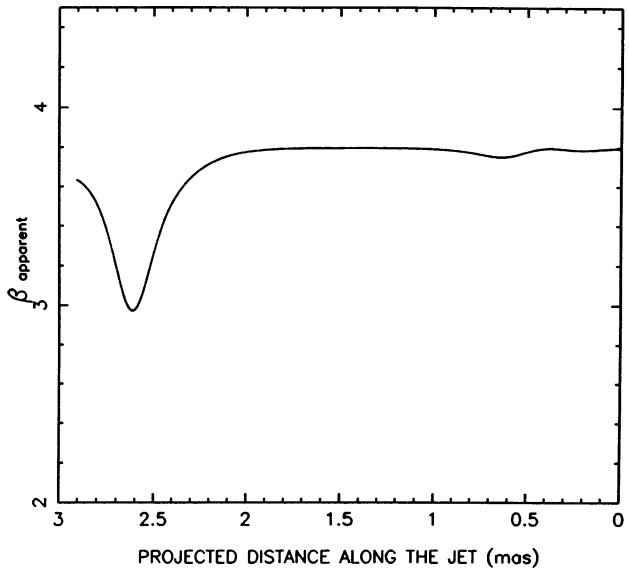

FIG. 5.—Variation of the apparent velocity of a feature moving down the jet as a function of distance along the jet for the geometry shown in Fig. 4. Shock wave velocity $\beta_{sh} = 0.967$.

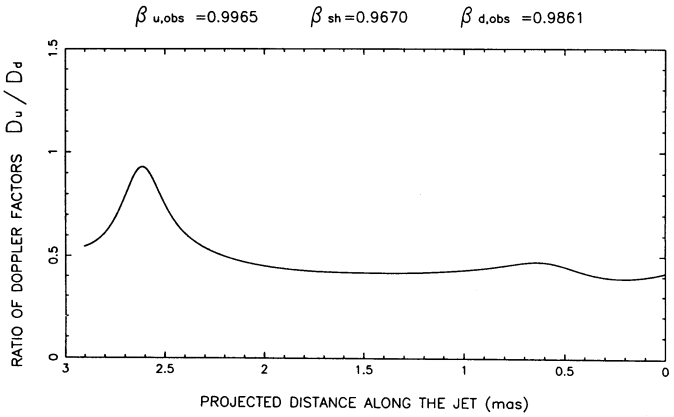

FIG. 6.—Ratio of velocities between the shocked and unshocked regions for the geometry shown in Fig. 4 considering $\beta_{u,obs} = 0.9965$ and $\beta_{d,obs} = 0.9861$.

do not provide the right boosting and relative intensity between the components. On the other hand, if we maintain the values for the compression ratio and for the upstream velocity in the observer's frame, $\beta_{u,obs} = 0.9965$, we obtain for the shock front velocity $\beta_{sh} = 0.9993$, which provides much larger apparent velocities than measured observationally. We point out, however, that the perhaps inappropriate use of an ultrarelativistic equation of state defines the relation between $\beta_{u,obs}$ and β_{sh}. Forward shocks should therefore not be discarded on the basis of our modeling.

In Figure 7 we show several steps in the shock wave evolution—associated with the evolution of component *b*—along the jet. They correspond to shock wave positions along the jet $d_{sh,i} = 20$, 27, and 31 pc that are associated with the projected positions on the sky $d_{sh,i} = 8$, 10, and 11 pc, respectively. (The linear to angular scale translates as follows:

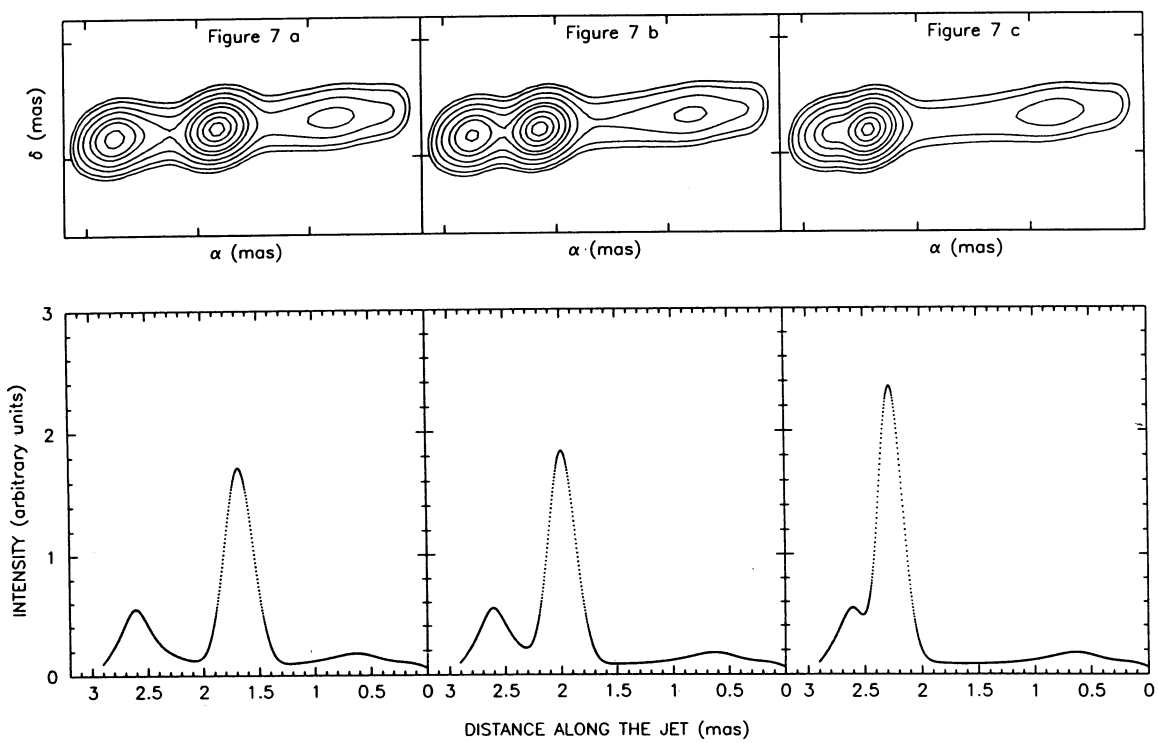

FIG. 7.—Intensity as a function of position in the jet at a wavelength of $\lambda = 1.3$ cm for shock waves placed at jet positions (*a*) $d_{sh,i} = 20$ pc, (*b*) $d_{sh,i} = 27$ pc, and (*c*) $d_{sh,i} = 31$ pc. We have adopted the following physical parameters for the relativistic jet: Relativistic electron spectrum normalization $N_0 = 0.0001$ (cgs units); magnetic field along jet direction $B_{\parallel} = 0.016$ G; random magnetic field $B_{rand} = 5B_{\parallel}$; spectral index of the electron distribution, $s = 2.5$; opening angle of the jet $\phi = 4°$; jet length $L = 50$ pc; shocked region size $L_{sh} = 3$ pc; shock front velocity $\beta_{sh} = 0.967$; velocity of the unshocked flow in the observer's reference frame $\beta_{u,obs} = 0.9965$ and the geometry showed in Fig. 4. We consider that at the position $d = 0$ the jet width has some finite value. We show also the two-dimensional maps associated with each emission curve.

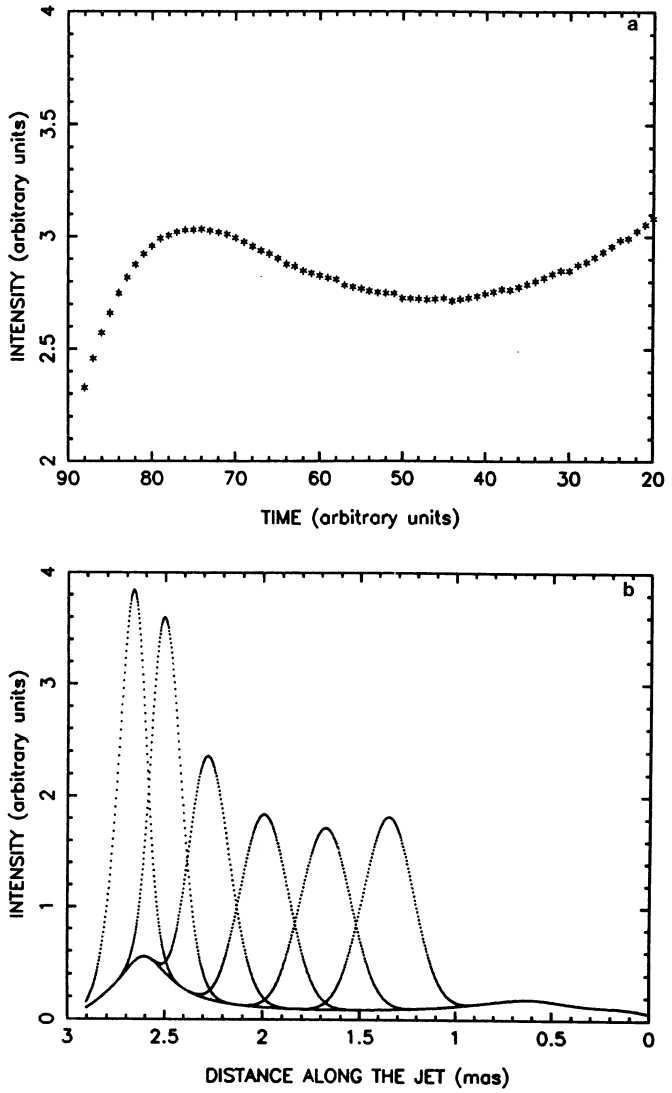

FIG. 8.—(*a*) Time evolution of the total flux density at wavelength $\lambda = 1.3$ cm for a shock wave traveling along the jet. We have considered the same physical parameters for the relativistic jet as in Fig. 7 and the geometry given in Fig. 4. (*b*) Intensity profiles corresponding to different shock wave positions along the jet.

1 mas $\leftrightarrow$ 3.99 pc.) We also show the two-dimensional brightness distribution associated with each of the light curves, obtained using the program MODPLOT of the Caltech VLB Package, kindly made available to us by T. J. Pearson. MODPLOT convolves the brightness distribution obtained by our code with a selected beam, producing the simulated source map.

The main results of our modeling are as follows:

1. The model total flux density at a wavelength of $\lambda = 1.3$ cm follows the time evolution shown in Figure 8, which corresponds well to the observed light curve: a decrease in the total flux density from 1980 to 1985 and an increase from 1985 on, approaching in 1991 the value that the flux density had in 1980. In Figure 8 we also show the time dependence of the emission of the jet while a shock wave advances along it. Comparison with Figure 7 gives the relations

$$S(d_{\rm sh} = 31 \text{ pc}) > S(d_{\rm sh} = 20 \text{ pc}) > S(d_{\rm sh} = 27 \text{ pc}) .$$

The amplitude of the shocked area emission profiles diminishes during the first years due to the expansion of the jet (from $d_{\rm sh} = 20$ pc to $d_{\rm sh} = 27$ pc); however, from 1985 on, the amplitude of the profiles increases progressively due to enhanced beaming owing to geometric effects (from $d_{\rm sh} = 27$ pc to $d_{\rm sh} = 31$ pc).

2. The stability of the relative distance between components *a* and *c* is explained as the emission from two physically fixed positions. Hardee (1990) has shown that macroinstabilities in the fluid can induce a jet to bend by several degrees. Bends in a relativistic jet produce variations in the Doppler boosting, and therefore changes in the brightness distribution. At the positions associated with components *a* and *c*, the jet bends by a few degrees toward the observer, enhancing the brightness at these positions. The deceleration of component *b* as its flux density increases is explained as a consequence of a progressively more parallel orientation of the jet axis relative to the line of sight (see Fig. 4) such that θ becomes less than the angle corresponding to maximum apparent superluminal motion $\theta(\beta_{\rm app} = \max) = \sin^{-1}(1/\gamma)$. As the jet curves toward the observer, the Doppler boosting factor both of the quiescent and the shocked flow are enhanced; hence, component *b* becomes brighter as it travels down this section as the apparent superluminal motion decreases.

3. Component *d*, which corresponds to the narrow end of the jet, is present in the model two-dimensional intensity maps and in the brightness profiles along the jet. This component could be the core of the radio source, whose intrinsic emission would be much reduced due to the orientation effects. We show in Figure 9*a*, to compare with the observations at $\lambda = 1.3$ cm (Fig. 1*a*), the simulated time evolution of the total flux density of 4C 39.25. We show in Figure 9*b* the emission profiles of the jet at different positions of the shock wave moving along the jet. We show in Figure 10 the simulated two-dimensional intensity maps at $\lambda = 2.8$ cm. They correspond to different steps in the evolution of the shock wave toward the position of *a*. These maps compare well with the observed images shown in Figure 1. Note that component *d* does not appear in either the simulated or the observed maps at $\lambda = 2.8$ cm. This is consistent with the assumed self-absorbed character of this component.

This model and its characteristic set of parameters is the best we have found within plausible a priori values, obtained from observational results, and fine-tuned a posteriori. The values of some of the physical parameters are very well constrained, but for some others there is a range of possible values. For example, the opening angle is restricted to lie between 3° and 5°; the velocity of the quiescent nonshocked flow lies between $0.996c$ and $0.997c$; and the velocity of the shock front has a value between $0.965c$ and $0.970c$. We have executed multiple iterations of our computer code to find the best values of the 4C 39.25 simulation, since the adjustment of one parameter clearly requires the readjustment of another one. We have made a sensitivity analysis of our best solution that confirms that the given ranges for the physical parameters are the most appropriate ones over the regions of parameter space explored by our simulations.

4.4. *Alternative Model*

There is another possible scenario in which the change in jet width can be interpreted as due to changing physical conditions in the jet or surrounding medium. Daly & Marscher (1988) presented a model of a pressure-confined relativistic

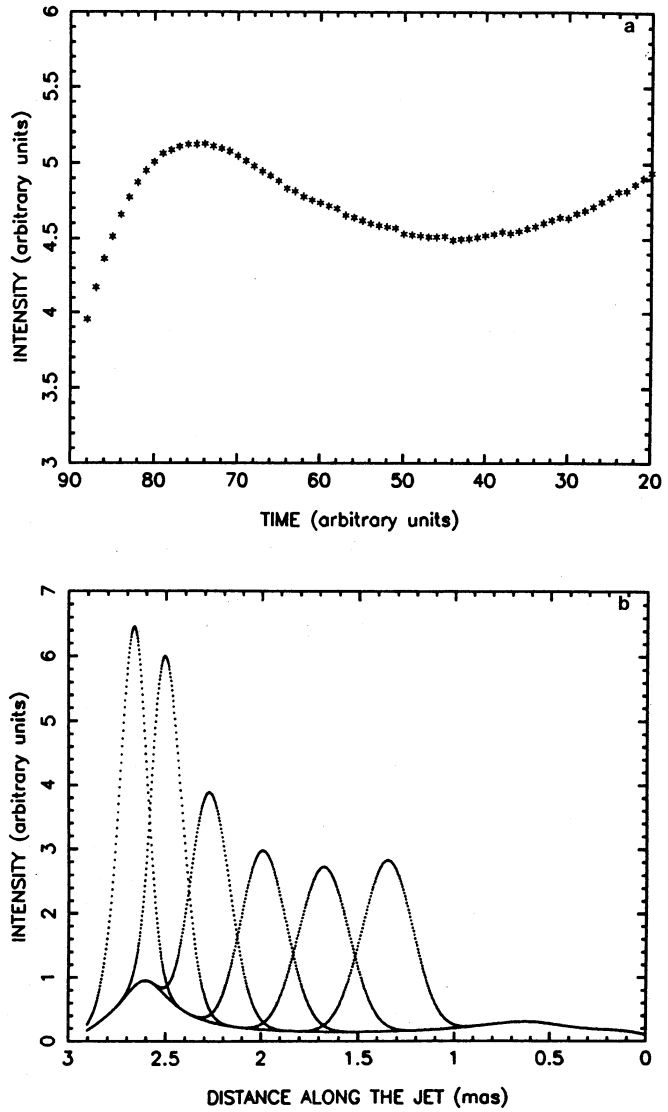

FIG. 9.—(*a*) Time evolution of the total flux density at wavelength $\lambda = 2.8$ cm, for a shock wave traveling along the jet. We have considered the same physical parameters for the relativistic jet as in Fig. 7 and the geometry given in Fig. 4. (*b*) Superposition of intensity profiles corresponding to different shock wave positions along the jet.

nonmagnetized jet based on classical hydrodynamics. This class of models is able to explain the coexistence of superluminal and stationary jet components and the change of β_{app} with jet width. The change in opening angle is either explained by a change in the ratio between the external pressure and the pressure inside the jet or, in the case that the pressure ratio is constant, by a change in the velocity of the propagating shock. In the Daly & Marscher model, in the regions where the jet broadens an increase in the apparent superluminal velocity is expected. This is in contrast to what we observe. We present in Figure 11 the deconvolved transverse width of the jet $\mathrm{FWHM}_{dec} = (\mathrm{FWHM}^2 - \mathrm{BEAM}^2)^{1/2}$, where BEAM is the FWHM of the restoring beam as a function of the distance along the jet. (The jet width is obtained from the program MAPANA, kindly made available to us by C. A. Hummel; the program computes the size of slices across the jet in order to determine the FWHM of the jet at the position of the slice by fitting a Gaussian curve to the profile). We show, for some of the observations analyzed within this paper, that the jet width reaches a minimum at the position of component *b*, the superluminal component, and reaches a maximum at the positions of the stationary components, *a* and *c*.

5. CONCLUSIONS

We have studied the parsec-scale radio jet of 4C 39.25. We have analyzed different observing epochs at wavelengths $\lambda = 1.3$, 2.8, and 3.6 cm. These maps have clarified the structure and kinematics of 4C 39.25. The source consists of a curved jet, as suggested from the nonuniform proper motion of the superluminal component, the relative position angles between the different components, and the time evolution of the total flux density emanating from a previously undetected core. We have detected a new component, *d*, at $\lambda = 1.3$ cm. This component is a plausible candidate to be the "core" of the radio source, although the possibility of a recurrent phenomenon—with *d* being a new superluminal component—cannot yet be excluded.

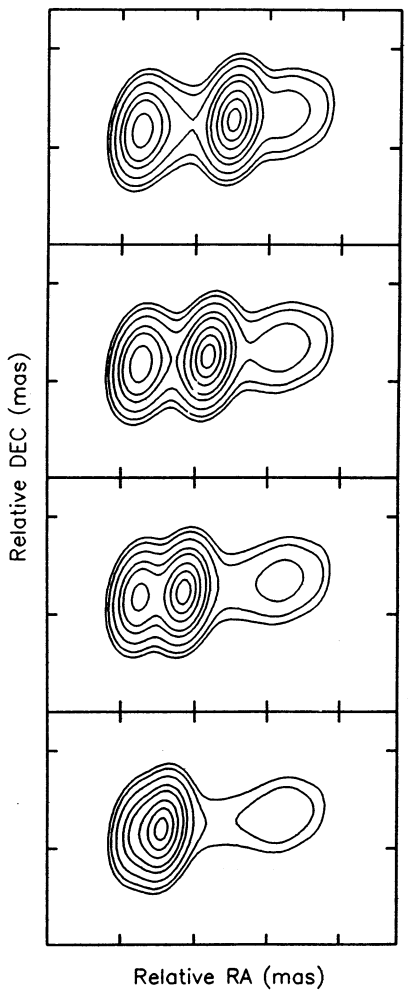

FIG. 10.—Simulated two-dimensional maps of the radio source 4C 39.25 at wavelength $\lambda = 2.8$ cm. We have considered the same physical parameters for the relativistic jet as in Fig. 7 and the geometry given in Fig. 4. The simulated maps correspond approximately to the observed maps at epochs 1983.5, 1986.3, 1987.7, and 1988.7 (cf. Fig. 1*b*).

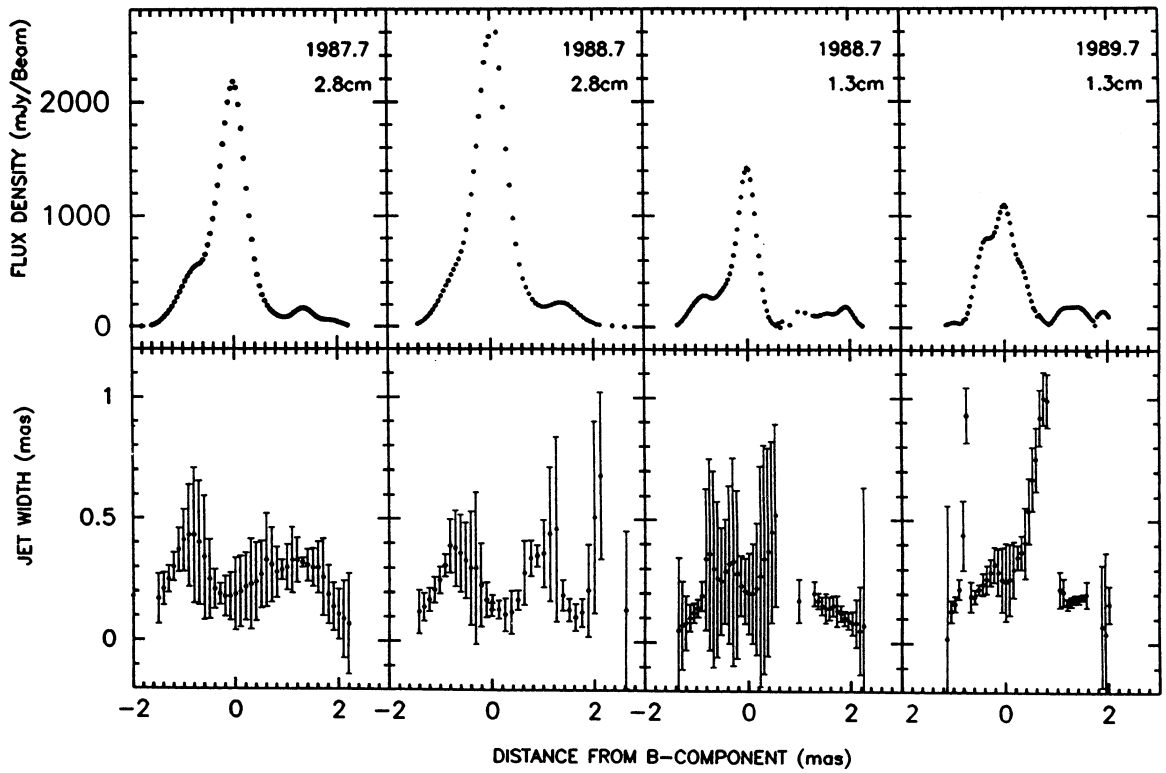

FIG. 11.—*Bottom panels*: Jet width vs. distance along the jet obtained by deconvolving the beam from the maps at $\lambda = 1.3$ and 2.8 cm (Figs. 1*a* and 1*b*) at several epochs. For reference, the positions of the peaks in intensity can be obtained from the model one-dimensional brightness distribution along the jet axis shown in the top panels.

We have analyzed the structure of a superluminal source in terms of shock waves traveling along a supersonic jet. If a shock wave is present in the parsec-scale jet of a radio source, it will produce an enhancement of the magnetic field and of the particle density, thereby increasing the emissivity and forming a superluminal component in the relativistic jet. The boosting effects are determined as a function of the velocity of the shock front with respect to the observer and of the flow velocity with respect to the shock front, and is therefore different for the shocked region and the quiescent region. We can explain the existence of stationary compact components through bends in the jet. A curvature in a relativistic jet leads to variations in the Doppler boosting that appear as components in the parsec-scale radio jet observed with VLBI.

We have found a geometry and a set of physical parameters that reproduce the structure of 4C 39.25. The model explains the stationarity of components *a* and *c* as being locations of changes in the jet orientation relative to the observer, and the kinematics of component *b* in terms of a moving shock wave. The bends in the jet can produce the observed change in the apparent superluminal speed as well as variations in the flux density and in the spectral index of component *b*.

We thank the staff at the participating observatories for carrying out our *in absentia* VLBI observations. Haystack Observatory, Owens Valley Radio Observatory, Hat Creek Radio Observatory, and the Fort Davis antenna of the Harvard College Observatory were funded by the US National Science Foundation. The National Radio Astronomy Observatory is operated by Associated Universities Inc., under cooperative agreement with the US National Science Foundation. A. P. M. and Y. F. Z. gratefully acknowledge partial support by the US National Science Foundation through grant AST-8815848. This work was supported in part by the Spanish DGICYT grants PB86-0616 and PB89-0009. We would like to thank H. Blaschke, H. Lüdecke, and U. Stürsberg for operating the Bonn correlator and their patient help during the correlation, and the Mk II correlator group in Caltech for similar support.

REFERENCES

Alberdi, A. 1991, Ph.D. thesis, Universidad de Granada, Spain
Alberdi, A., Marcaide, J. M., Elósegui, P., Schalinski, C. J., & Witzel, A. 1990, in Proc. 7th Work. Meeting on European VLBI, ed. A. Rius (Madrid: CSIC Publications), 154
Alef, W., & Porcas, R. W. 1986, A&A, 168, 365
Aller, H. D., Aller, M. F., Latimer, G. E., & Hodge, P. E. 1985, ApJS, 59, 513
Bååth, L. B., et al. 1980, A&A, 86, 364
Biretta, J. A., & Cohen, M. H. 1987 in Superluminal Radio Sources, ed. J. A. Zensus & T. J. Pearson (Cambridge: Cambridge Univ. Press), 40
Blandford, R. D., & Königl, A. 1979, ApJ, 232, 34
Blandford, R. D., & McKee, C. F. 1976, Phys. Fluids, 19, 1130
Clark, B. G. 1973, Proc. IEEE, 61, 1242
Cornwell, T. J., & Wilkinson, P. N. 1981, MNRAS, 196, 1067
Daly, R. A., & Marscher, A. P. 1988, ApJ, 334, 539
Hardee, P. E. 1990 in Parsec-Scale Radio Jets, ed. J. A. Zensus & T. J. Pearson (Cambridge: Cambridge Univ. Press), 266
Hewitt, A., & Burbidge, G. 1980, ApJS, 43, 57
Högbom, H. 1974, A&AS, 15 (3), 417
Hughes, P. A., Aller, H. D., & Aller, M. F. 1989, ApJ, 341, 54
———. 1990, in Parsec-Scale Radio Jets, ed. J. A. Zensus & T. J. Pearson (Cambridge: Cambridge Univ. Press), 250
Jackson, N. 1990, Ph.D. thesis, Manchester University
Königl, A. 1980, Phys. Fluids, 23, 1083
Kollgaard, R. I., Wardle, J. F. C., & Roberts, D. H. 1990, AJ, 99, 1057

Marcaide, J. M., et al. 1990, in Parsec-Scale Radio Jets, ed. J. A. Zensus & T. J. Pearson (Cambridge: Cambridge Univ. Press), 59
Marcaide, J. M., Alberdi, A., Elósegui, P., Schalinski, C. J., Jackson, N., & Witzel, A. 1989, Astron. Astrophys., 211, L23
Marcaide, J. M., et al. 1985, Nature, 314, 424
Marscher, A. P. 1990, in Parsec-Scale Radio Jets, ed. J. A. Zensus & T. J. Pearson (Cambridge: Cambridge Univ. Press), 236
Marscher, A. P., Gear, W. K., & Travis, J. P. 1990, in Variability of Blazars, ed. E. Valtaoja & M. Valtonen (Cambridge: Cambridge Univ. Press), 85
Marscher, A. P., Shaffer, D. B., Booth, R. S., & Geldzahler, B. J. 1987, ApJ, 319, L69
Marscher, A. P., Zhang, Y. F., Shaffer, D. B., Aller, H. D., & Aller, M. F. 1991, ApJ, 371, 491
Pauliny-Toth, I. I. K., Preuss, E., Witzel, A., Graham, D., Kellermann, K. I., & Ronnag, B. 1981, AJ, 86, 371
Pearson, T. J., & Readhead, A. C. S. 1984, in IAU Symp. 110, VLBI and Compact Radio Sources, ed. R. Fanti, K. Kellermann, & G. Setti (Dordrecht: Reidel), 15
Pearson, T. J., & Readhead, A. C. S. 1988, ApJ, 328, 114
Rogers, A. E. E., et al. 1983, Science, 219, 51
Schalinski, C. J., Alberdi, A., Elósegui, P., & Marcaide, J. M. 1988, in IAU Symp. 129, The Impact of VLBI on Astrophysics and Geophysics, ed. M. J. Reid & J. M. Moran (Dordrecht: Kluwer), 39
Schalinski, C. J., Witzel, A., Alef, W., Campbell, J., & Alberdi, A. 1990, in Proc. 7th Work. Meeting on European VLBI, ed. A. Rius (Madrid: CSIC Publications), 121
Shaffer, D. B., et al. 1977, ApJ, 218, 353
Shaffer, D. B., Marscher, A. P., Marcaide, J. M., & Romney, J. D. 1987, ApJ, 314, L1
Tang, G., Ronnang, B., & Bååth, L. B. 1987, A&A, 185, 87
Zensus, A. J., & Pearson, T. J., ed. 1990, Parsec-Scale Radio Jets (Cambridge: Cambridge Univ. Press), 66
Zhang, Y. F., Marscher, A. P., Shaffer, D. B., Marcaide, J. M., Alberdi, A., & Elósegui, P. 1990, in Parsec-Scale Radio Jets, ed. J. A. Zensus & T. J. Pearson (Cambridge: Cambridge Univ. Press), 66